Supplementary Information

Upstream Wall Vortices in Viscoelastic Flow Past a Cylinder.

Cameron C. Hopkins, Simon J. Haward, and Amy Q. Shen

Okinawa Institute of Science and Technology Graduate University,

Onna-son, Okinawa, 904-0495, Japan

(Dated: June 14, 2022)

I. SIDE-VIEW CHARACTERIZATION OF THE WALL VORTICES

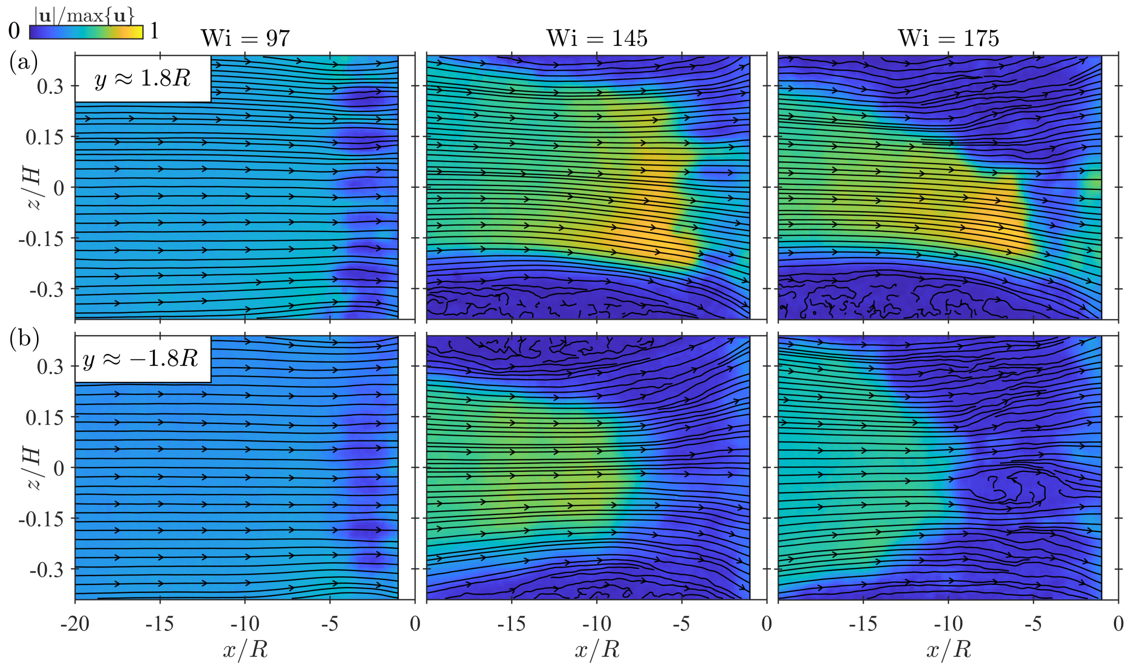

FIG. S1. Time-averaged velocity fields for the flow of the wormlike micellar solution past the microcylinder imaged in the x-z planes (a) $y \approx 1.8R$ and (b) $y \approx -1.8R$ at (left) Wi = 97, (center) Wi = 145, and (right) Wi = 175.

To investigate the structure of the wall vortices along the height of the channel (in the z direction), we performed select μPIV flow experiments with the channel oriented such that the $x - z$ plane could be imaged. At a given flow rate, 500 frame pairs were recorded at 50 pairs per second focused on the $y \approx 1.8R$ plane before changing the focus while maintaining the flow to the $y \approx -1.8R$ plane and recording another 500 frame pairs. Although the data at each Wi were recorded in a continuous flow experiment, they are not coincident, so it is not possible to make a direct comparison between the structure of the vortices in each plane especially when the flow is time dependent.

Time-averaged velocity fields at three values of Wi are shown in Fig. S1. The left column of Fig. S1 shows velocity fields at Wi $= 97 <$ Wi$_{c3}$, similar to the case shown in Fig. 3(c) in the main text. There are several relatively small vortices stacked in the z direction on both walls. The accompanying time dependent video (Movie S6) shows that in the $y \approx 1.8R$ plane, the number and position of the vortices remains constant in time. In the $y \approx -1.8R$

plane, the vortices shift in the z direction and merge or split over time. This time dependence is seemingly random.

The center column of Fig. S1 shows velocity fields at $\mathrm{Wi} = 145 > \mathrm{Wi}_{c3}$, greater than but near to the transition to time dependence and when the vortices are asymmetric in size, similar to the case shown in Fig. 5(a) and 7(b) in the main text. There are two relatively large vortices on the top and bottom walls of the channel ($z = \pm H/2$) that change size over time and can grow to fill nearly 35% of the channel height. In the $y \approx 1.8R$ plane, there are several relatively small vortices stacked in the z direction, similar to the case at lower Wi. In the $y \approx -1.8R$ plane, there is a larger seemingly symmetric vortex spanning the height of the channel, connecting with the vortices on the top and bottom walls. The accompanying time-dependent video (Movie S7) shows long-time variation in the position and size of the vortices in both planes along with more rapid pulsing in the x direction. In the $y \approx 1.8R$ plane the smaller vortices shift in the z direction and occasionally merge to form larger vortices. In the $y \approx -1.8R$ plane there are moments in time where one, or two, distinct larger vortices can be discerned that also shift in the z direction and merge or split.

The right column of Fig. S1 shows velocity fields at $\mathrm{Wi} = 175 > \mathrm{Wi}_{c3}$, also when the flow is time dependent, and the vortices are asymmetric in size similar to the case shown in Fig. 3(d) in the main text. The asymmetric shape of the vortices in both planes remain approximately constant in time. The accompanying video (Movie S8) shows that both vortices pulse periodically in the x direction.

II. RHEOLOGICAL CHARACTERIZATION OF THE SUPPLEMENTARY TEST FLUIDS

To investigate the effect of fluid rheology on the behavior of the flow past the microcylinder, we performed cursory flow experiments using three rheologically distinct test fluids. First, a weakly elastic, shear-thinning fluid comprised of 1000 ppm Xanthan Gum (4 MDa) in a solvent of 82 wt.% glycerol in water, labeled XG. Second, a more elastic, shear-thinning fluid comprised of 500 ppm Hydrolyzed Polyacrylamide in a solvent of 82 wt.% glycerol in water, labeled HPAA. Third, an elastic, approximately constant-viscosity Boger fluid comprised of 2000 ppm Polyethylene Oxide (4 MDa) in a solvent of 50 wt.% glycerol in water, labeled PEO. All reagents were acquired from Sigma Aldrich.

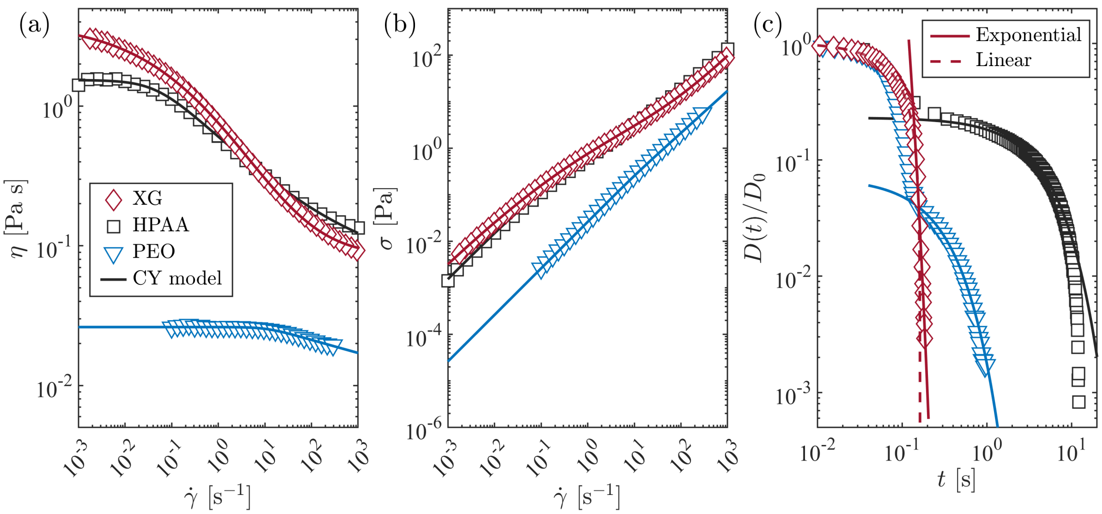

FIG. S2. Rheological characterization of the three test fluids described in the text. (a) Steady shear viscosity η and (b) shear stress σ *vs* $\dot{\gamma}$ with fits of the Carreau-Yasuda model. (c) Normalized filament diameter $D(t)/D_0$ *vs* t during capillary thinning in a CaBER device with fits of an exponential function (solid lines) to the measurements for each fluid, and a linear fit (dashed line) to the XG test fluid measurement.

The steady-shear and extensional rheology of the XG and HPAA solutions were measured at $T = 24$ °C using an Anton-Paar MCR502 stress-controlled rotational rheometer fitted with a 50 mm diameter 1° cone-and-plate fixture. For the PEO solution, a Couette cell fixture was used due to the fluid's relatively low viscosity. The inner cylinder of the Couette cell has radius 13.328 mm and height 39.984 mm. The fixed outer cylindrical cup has radius 14.459 mm. The steady shear viscosity η and shear stress σ are plotted *vs* $\dot{\gamma}$ in Fig. S2 (a) and (b), respectively. The flow curves (η *vs* $\dot{\gamma}$) for each fluid are well described by the

TABLE S2. Rheological properties of the three test fluids. The asterisk next to '2' for the PEO solution indicates that this parameter was fixed in the fitting, as described in the text

Fluid	η_0 [Pa s]	η_∞ [Pa s]	$\dot{\gamma}_c$ [s^{-1}]	n	a	λ [s]
HPAA	1.5	0.068	0.048	0.67	1.2	1.4
XG	4.0	0.084	0.38	0.28	0.36	0.0037
PEO	0.021	0.0024	11.2	0.89	2*	0.091

Carreau-Yasuda Generalized Newtonian fluid model given by

$$\eta = \eta_\infty + (\eta_0 - \eta_\infty)(1 + (\dot{\gamma}/\dot{\gamma}_c)^a)^{(n-1)/a}, \tag{1}$$

where η_∞ is the high shear-rate plateau viscosity, η_0 is the low shear-rate plateau viscosity, γ_c is the critical shear rate for the onset of shear thinning, n is the power-law index in the shear-thinning region, and a is a parameter that governs the rate of transition between the low shear-rate constant viscosity region and the shear-thinning region of the flow curve. Results of the fitting of Eq. 1 to the flow curves for each fluid are included in Table S2. Although the XG and HPAA solutions are shear thinning, and exhibit remarkably similar shear thinning behavior, neither fluid exhibits shear banding behavior, evident in Fig. S2 (b). Note that for the PEO solution flow curve the simplified form of the Carreau-Yasuda model was used where $a = 2$ is fixed, known as the Carreau model, to ensure the fitting routine yielded physically valid parameters.

The relaxation times of the fluids were measured via capillary thinning in a Capillary Breakup Extensional Rheometer (CaBER). The normalized mid-filament diameters $D(t)/D_0$ are plotted *vs* t in Fig. S2 (c), where $D_0 = 6$ mm is the initial diameter of the filament. After an initially rapid viscous thinning, the diameter of each filament thins exponentially with time in the elasto-capillary regime. In the elasto-capillary regime, the filament thinning is well-described by an exponential of the form

$$D(t) = Ae^{-t/3\lambda}, \tag{2}$$

where A is a constant and λ is the fluid relaxation time. Eq 2 was fit to the data and are shown as the solid lines in Fig. S2 (c). The relaxation times for each fluid are included in Table S2.

The thinning of the XG fluid filament follows a nearly Newtonian linear decay (dashed line in Fig. S2 (c))

$$D(t) = B(t_c - t), \tag{3}$$

where B and t_c are constants. For a short span of time near the breakup time of the filament the filament thins exponentially and deviates from the Newtonian thinning.

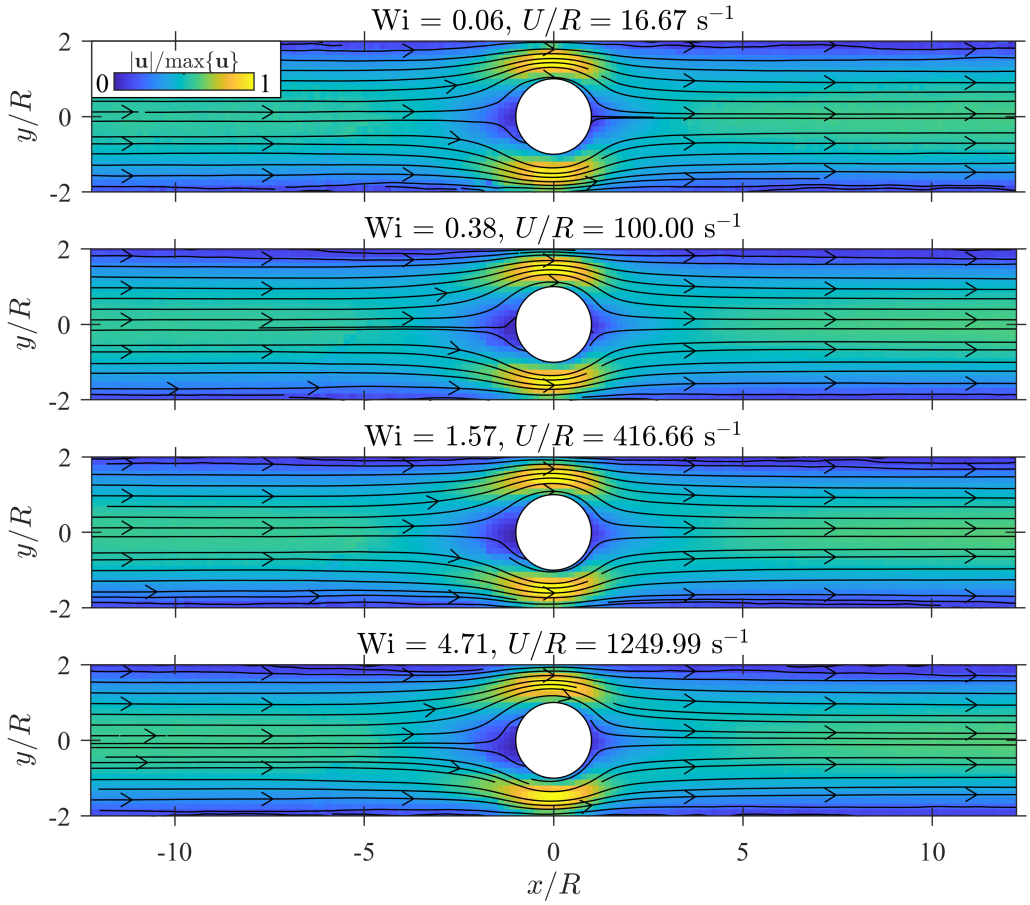

FIG. S3. Evolution of velocity fields with Wi for the XG solution flowing past the $B_R = 0.5$ microcylinder.

III. FLOW EXPERIMENTS

The flow experiments shown here followed the same procedure as detailed in the main text. For all velocity fields shown, 250 frame pairs were recorded at 25 pairs per second at each Wi. The flow rate was held for at least one minute prior to data collection.

A. Weakly elastic, shear-thinning fluid

Flow fields for the XG solution at various Wi $= U\lambda/R$ are shown in Fig. S3. At all of the Wi tested, no change in the flow behavior was observed. Due to the very small relaxation time of this fluid and the limit for how short the time separation can be between laser pulses in the PIV apparatus, the highest Wi attainable was Wi $= 4.71$. The characteristic shear rates imposed were $16.67 < U/R < 1250\ \mathrm{s}^{-1}$, which span the higher-shear-rate half of the shear thinning region of the flow curve for this solution (Fig. S2 (a)). Therefore, we conclude that shear thinning alone is not sufficient to cause the bending streamline instability and the formation of upstream wall vortices observed in this work.

B. Elastic, shear-thinning fluid

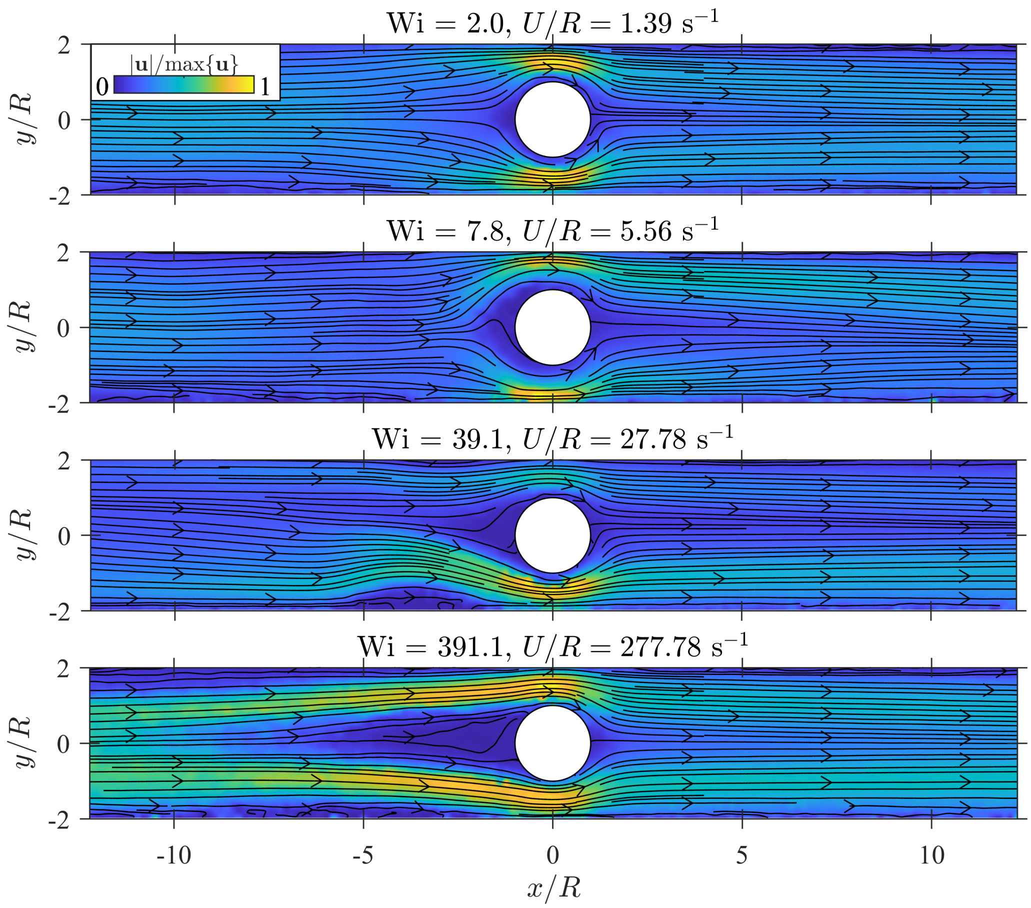

FIG. S4. Evolution of velocity fields with Wi for the HPAA solution flowing past the $B_R = 0.5$ microcylinder.

Flow fields for the HPAA solution at various Wi are shown in Fig. S4. With increasing Wi, the elastic flow instability progresses in an analogous manner to the wormlike micellar solution. At low Wi = 5, the flow is steady and laterally symmetric, with a slight fore-aft asymmetry presumably arising from the influence of extension at the downstream stagnation point of the cylinder. At slightly higher Wi = 20, the flow is steady with bent streamlines near the upstream stagnation point of the cylinder. At Wi = 100, there are vortices attached to the walls upstream of the cylinder. Finally, at Wi = 1000, there is a large vortex attached to the upstream pole of the cylinder. The time-dependent behavior of the flow was not investigated in these cursory experiments. Although the HPAA and XG solutions have very similar shear thinning properties, the flow instability is observed for the HPAA solution but not the XG solution. Therefore we conclude that suitable elasticity in the fluid is required for the instability to occur. These results also demonstrate that shear-banding is not a required rheological feature of the fluid to induce the observed flow instability we have reported. A more detailed parametric study to vary the degree of shear thinning and elasticity in the test fluids would be instructive.

C. Elastic, approximately constant-viscosity fluid

Flow fields for the PEO solution at various Wi are shown in Fig. S5. In stark contrast to the previous two cases, the flow evolves in a very different manner. No disturbance is observed upstream of the cylinder. Instead, a wake of slow moving fluid forms downstream of the cylinder that grows in length with increasing Wi. These results further support our supposition that shear thinning viscosity *and* elasticity are required for the upstream instability to occur in this system. Elasticity alone is insufficient, and it modifies the flow downstream of the cylinder.

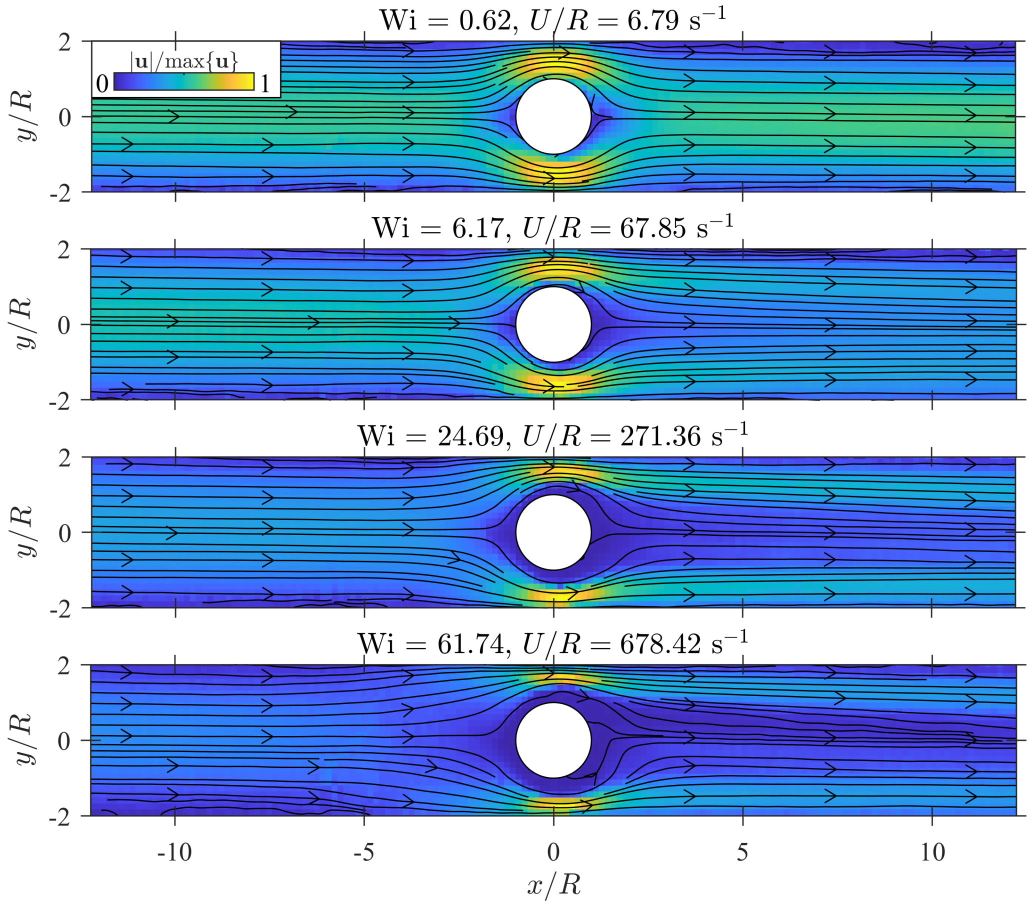

FIG. S5. Evolution of velocity fields with Wi for the PEO solution flowing past the $B_R = 0.5$ microcylinder.

IV. MOVIES

The following movies illustrate the time-dependent velocity fields for the flow of the wormlike micellar solution past the microcylinder at the Wi listed. Links to the movies can be found on the journal website. For reference, Wic1 is the critical Wi for the onset of the upstream bending streamline instability, Wic2 is the critical Wi for the formation of upstream wall-attached vortices, Wic3 is the critical Wi for the onset of time dependence, and Wic4 is the critical Wi for the significant growth of the upstream cylinder vortex.

Movie S1 Particle images and calculated velocity field at Wic1 ¡ Wi = 38 ¡ Wic2, at z = 0 plane, the same case as shown in Fig. 3 (b) in the main text. This is time-steady flow within the regime where there are bending streamlines upstream of the cylinder but no wall vortices.

Movies S2-S5 are at the same Wi as shown in Fig. 7 in the main text. These videos show the time-dependent velocity field along with the time series of $|v_p/U|$, χ, $\mathcal{W}$, and $\mathcal{L}$.

Movie S2 - $\mathrm{Wi}_{c2} < \mathrm{Wi} = 90 < \mathrm{Wi}_{c3}$ at the $z = 0$ plane. Time-steady with small wall vortices.

Movie S3 - $\mathrm{Wi}_{c3} < \mathrm{Wi} = 148 < \mathrm{Wi}_{c4}$ at the $z = 0$ plane. Time-dependent with small wall vortices at a Wi near the initial transition to time dependence.

Movie S4 - $\mathrm{Wi}_{c3} < \mathrm{Wi} = 190 < \mathrm{Wi}_{c4}$ at the $z = 0$ plane. Time-dependent with asymmetric wall vortices at a higher Wi than in Movie S3.

Movie S5 - $\mathrm{Wi} = 507 > \mathrm{Wi}_{c4}$ at the $z = 0$ plane. Time-dependent at a Wi within the cylinder vortex regime.

Movies S6-S8 show the time-dependent velocity fields recorded in the x-z plane at the positions $y \approx \pm 1.8R$ to illustrate how the wall vortices are shaped and behave in the z direction. The movies correspond to the time-averaged velocity fields shown in Fig. S1. Note that the videos were not recorded coincidentally at a given Wi, so it is not possible to directly compare the shape of the vortices and time-dependent behaviour between the two planes in each video.

Movie S6 - $\mathrm{Wi}_{c2} < \mathrm{Wi} = 97 < \mathrm{Wi}_{c3}$ at the $y \approx \pm 1.8R$ planes. Approximately time-steady small wall vortices.

Movie S7 - $\mathrm{Wi}_{c3} < \mathrm{Wi} = 145 < \mathrm{Wi}_{c4}$ at the $y \approx \pm 1.8R$ planes. Time-dependent asymmetric wall vortices.

Movie S8 - $\mathrm{Wi}_{c3} < \mathrm{Wi} = 175 < \mathrm{Wi}_{c4}$ at the $y \approx \pm 1.8R$ planes. Time-dependent asymmetric wall vortices at slightly higher Wi than in Movie S7.